Science
AAAS

Multiscale Mechanics of Fibrin Polymer: Gel Stretching with Protein Unfolding and Loss of Water

André E. X. Brown, *et al.*

Science **325**, 741 (2009);
DOI: 10.1126/science.1172484

Science (print ISSN 0036-8075; online ISSN 1095-9203) is published weekly, except the last week in December, by the American Association for the Advancement of Science, 1200 New York Avenue NW, Washington, DC 20005.

Multiscale Mechanics of Fibrin Polymer: Gel Stretching with Protein Unfolding and Loss of Water

André E. X. Brown,[1,2] Rustem I. Litvinov,[3] Dennis E. Discher,[2,4] Prashant K. Purohit,[5] John W. Weisel[3]*

Blood clots and thrombi consist primarily of a mesh of branched fibers made of the protein fibrin. We propose a molecular basis for the marked extensibility and negative compressibility of fibrin gels based on the structural and mechanical properties of clots at the network, fiber, and molecular levels. The force required to stretch a clot initially rises linearly and is accompanied by a dramatic decrease in clot volume and a peak in compressibility. These macroscopic transitions are accompanied by fiber alignment and bundling after forced protein unfolding. Constitutive models are developed to integrate observations at spatial scales that span six orders of magnitude and indicate that gel extensibility and expulsion of water are both manifestations of protein unfolding, which is not apparent in other matrix proteins such as collagen.

Fibrin clots are proteinaceous gels that polymerize in the blood as a consequence of biochemical cascades at sites of vascular injury. Together with platelets, this meshwork stops bleeding and supports active contraction during wound healing (*1*, *2*). Fibrin also provides a scaffold for thrombi, clots that block blood vessels and cause tissue damage, leading to myocardial infarction, ischemic stroke, and other cardiovascular diseases (*3*). To maintain hemostasis while minimizing the impact of thrombosis, fibrin must have suitable stiffness and plasticity (*4*), but also sufficient permeability so that the network can be effectively decomposed (lysed) by proteolytic enzymes (*5*, *6*). It is challenging to meet all of these conditions because open scaffolds would be expected to break at low strains, as is true for collagen gels (*7*). To address how fibrin clots are both permeable and highly extensible, we studied fibrin structures across multiple spatial scales, from whole clots to single fibers and single molecules (Fig. 1).

Fibrin clots were made from purified human fibrinogen under conditions (*8*) that resulted in the formation of long, straight fibers, similar to those found in physiological clots. To simplify the interpretation, the clots were covalently ligated with the use of a transglutaminase (blood clotting factor XIIIa), as naturally occurs in the blood, which prevents protofibrils from sliding past one another, thus eliminating persistent creep (*9*).

Measurements of the extensibility of 2-mm-diameter fibrin clots (Fig. 2A) demonstrated that the clots could be stretched to more than three times their relaxed length before breaking, with an average stretch of 2.7 ± 0.15–fold ($n = 6$) (*10*). This is comparable to the single-fiber extensibility that is observed when a fibrin fiber is laterally stretched with an atomic force microscope (*11*). Qualitatively, the resulting force-strain curve for fibrin is similar to those observed for rubbers and other materials made from flexible chains (*12*). However, for fibrin clots, which are made of longer, straighter fibers than the thermally fluctuating polymer chains in rubber, models of rubber-like elasticity predict a branching density that is wrong by seven orders of magnitude (*4*). Therefore, new models are needed to understand clot mechanics.

In addition to the large extensibility of fibrin clots, these gels also displayed a dramatic decrease in volume upon stretching [supporting online material (SOM) movie S1], unlike most rubbery materials. This unusual effect is quantified in Fig. 2B where the lateral contraction of the gel λ_* allows one to calculate the relative volume ($\lambda_1\lambda_*^2$), which is plotted as function of strain (black circles) and contrasted with a volume-conserving incompressible material (black dashed line). The shrinkage of the stretched clot was due to water expulsion, as confirmed by an ~10-fold increase in the protein content in clots at a strain of 2 (fig. S1B). This protein concentrating effect, or syneresis, is mechanically induced and corresponds to a negative compressibility for the gel (Fig. 2B, inset); the intrinsic compressibility of proteins is usually positive and small, ~2×10^{-4} MPa^{-1} (Fig. 2B inset, open circle) (*13*). This effect might be related to the phenomenon of negative normal stress observed for networks of semiflexible polymers, because even though fibrin fibers are relatively stiff, it is still possible that they buckle more easily than they stretch, thus leading to an effective inward force (*14*). However, our data below support an alternative explanation in which the volume change is associated with protein unfolding and bundling of stretched fibrin fibers.

To understand what makes fibrin so different from other highly extensible polymers, including rubbers and hydrogels, we quantified the structural changes that occur in stretched clots at the network and fiber levels. Unstrained clots imaged with the use of scanning electron microscopy have well-separated fibers with an essentially random orientation (Fig. 3A, top image). When strain is applied (Fig. 3A, lower images), the fibers begin to align and the network orientational order parameter (*15*) increases gradually from 0.1 to 0.7 at a strain of ~2.5 (Fig. 3B).

Transmission electron microscopy of transverse sections through fibrin clots at increasing strain (Fig. 3C, insets) provides a clear picture

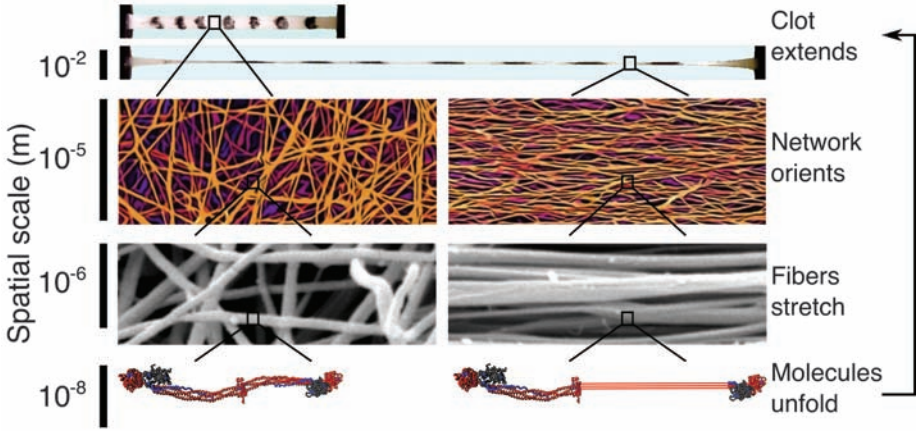

Fig. 1. Blood clots are highly extensible supramolecular protein polymers formed from well-separated, relatively straight and stiff fibers ~200 nm in diameter. When stretched (see movie S1), the fiber network aligns in the direction of the applied strain and the individual fibers stretch, forcing the fibrin monomers that make up the fibers to extend. Ultimately, it is this molecular unfolding that allows clots to stretch so far. Thus, understanding fibrin clot mechanics requires knowledge of the mechanical response and the corresponding structural changes spanning from the centimeter scale to the nanometer scale.

[1]Department of Physics and Astronomy, University of Pennsylvania, Philadelphia, PA 19104, USA. [2]Nano/Bio Interface Center, University of Pennsylvania, Philadelphia, PA 19104, USA. [3]Department of Cell and Developmental Biology, University of Pennsylvania School of Medicine, Philadelphia, PA 19104, USA. [4]Graduate Groups in Physics and Cell Biology and Physiology, University of Pennsylvania, Philadelphia, PA 19104, USA. [5]Department of Mechanical Engineering and Applied Mechanics, University of Pennsylvania, Philadelphia, PA 19104, USA.

*To whom correspondence should be addressed. E-mail: weisel@mail.med.upenn.edu

of how the fibers become thinner, closer together, and bundle. The area occupied by fibers increases from ~5 to 24% at a strain of 2 (Fig. 3C, graph). This increase is smaller than expected given the macroscopic shrinkage of the entire clot (see SOM), indicating that the volume decrease is a combined result of fiber bundling and a decrease in fiber diameter from 185 ± 36 to 74 ± 16 nm (mean ± SD, $P << 0.0001$, Student's t test). Similar transmission electron micrographs (although without corresponding scanning electron micrographs) of fiber ordering have been reported (*16*), but quantifying the strain dependence of these observations proves important below in constraining possible models. Furthermore, knowing the stress applied and the fractional cross section occupied by fibers allows for an estimate of the force per protofibril of ~75 pN at a strain of 2. Given the small loading rate that we used, this force is large enough to result in substantial unfolding of fibrin (*17*). Protein unfolding is generally associated with increased exposure of hydrophobic groups that would tend to interact (e.g., bundle) and expel water, as observed here.

The half-staggered packing of fibrin (Fig. 4A) leads to a ~22-nm repeat that can be measured by small-angle x-ray scattering (SAXS), and this measurement can be used as a readout of the molecular length (*18*). The position of the peak corresponding to the 22-nm spacing does not change substantially as the clot is stretched (Fig. 4B), ruling out a gradual extension of molecules during the stretch, which would otherwise increase this spacing, as suggested by Roska *et al*. (*19*). The marked increase in peak width that we observed indicates an increase in disorder that is consistent with an increasing number of molecules unfolding in response to the large strain. This increase in disorder is captured by the decrease in the Scherrer length L (Fig. 4C): The length over which the 22-nm repeat is correlated (*20*). A decrease in L indicates that the average size of the regions containing a consistent 22-nm repeat becomes smaller because of intervening regions of unfolded molecules. To control for the effect on L of fiber alignment that accompanies strain, we made magnetically prealigned samples in which the fibers were already oriented along the direction of applied strain. In this case, the decrease in L occurs at lower strains because fiber alignment cannot take up as much of the applied strain (Fig. 4C, blue circles). This change is reversible when fibers are allowed to relax (Fig. 4C, blue arrow). Similarly, to control for fiber sliding as an alternative mechanism of strain accommodation, we stretched samples that were not covalently ligated using factor XIIIa. Without ligation, protofibrils slide with respect to each other instead of stretching, and unfolding is suppressed (Fig. 4C, black circles). This behavior is expected for two-state extension in which some molecules extend completely while others remain folded, consistent with our earlier single-molecule observations of the forced unfolding of coiled coils

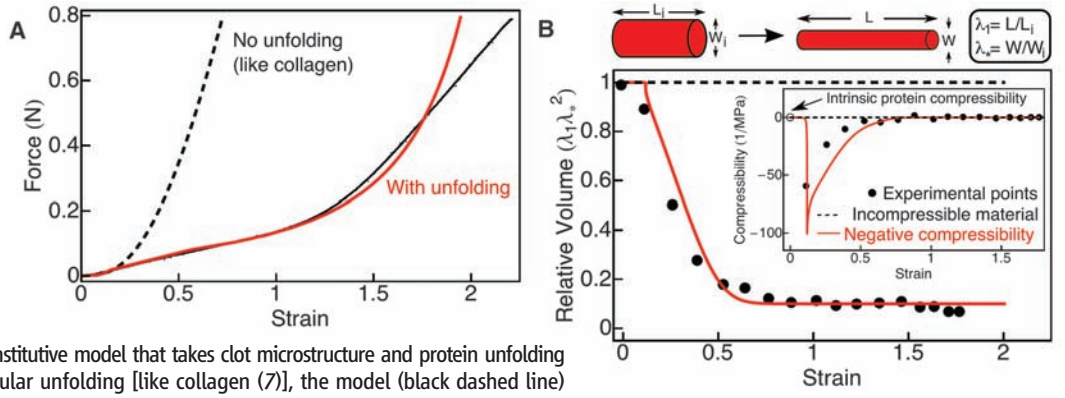

Fig. 2. (**A**) Representative force-extension curve of a cylindrical fibrin clot reaching a threefold longitudinal stretch. The average stretch before breaking was 2.7 ± 0.15–fold (mean ± SEM, $n = 6$ experiments). As the strain (stretched length/initial length − 1) increases, the force on the clot increases linearly until a strain of ~1.2 is reached, at which point the sample hardens and enters a new regime with a steeper slope (black solid line). The force-extension curve (black solid line) is fit using a constitutive model that takes clot microstructure and protein unfolding into account (red line). Without molecular unfolding [like collagen (*7*)], the model (black dashed line) rapidly diverges from the experimental data (black solid line). (**B**) The relative clot volume decreases with strain (black circles), in contrast to the behavior of an incompressible material (dashed black line). This decrease is predicted with the use of the same model and parameters that we used to fit the force-extension data (red line), demonstrating that the volume decrease occurs in parallel with molecular extension (SOM Eq. 29). A decreasing volume with increasing stretch corresponds to a negative compressibility (inset), which indicates that there is a source of free energy to drive contraction, possibly due to fiber bundling when hydrophobic side chains aggregate and bury after exposure during unfolding. The negative compressibility is a property of the network. Proteins in solution have been observed to have intrinsic compressibilities ~2×10^{-4} MPa^{-1} (open circle, inset) (*13*). L, length; L_i, initial length; W, width; W_i, initial width.

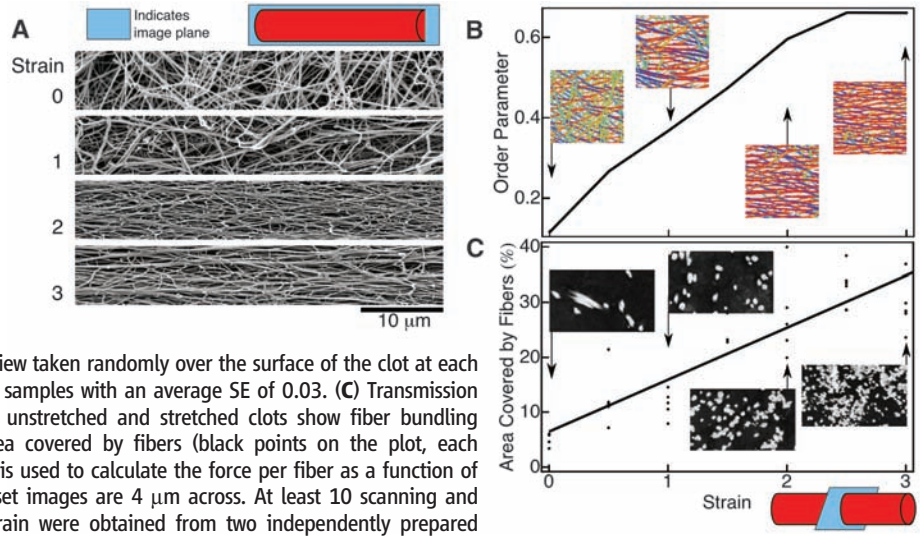

Fig. 3. Structural changes in stretched fibrin clots at the network and fiber levels. Scanning electron micrographs of stretched clots (**A**) show how the fibrin fibers align with strain. (**B**) These scanning electron micrographs are segmented using a Laplace of Gaussian filter that determines which pixels are fibers and which are background and also calculates the orientation θ at each fiber pixel. The inset images show the results of the segmentation with the color at each pixel corresponding to that pixel's orientation. These data are summarized as an orientational order parameter <cos(2θ)> that can range between 0 for randomly oriented fibers and 1 for perfectly aligned fibers (*14*). Data points are averages of five fields of view taken randomly over the surface of the clot at each strain. The order parameter was fairly uniform across samples with an average SE of 0.03. (**C**) Transmission electron micrographs of transverse sections through unstretched and stretched clots show fiber bundling (insets). The plot shows the total cross-sectional area covered by fibers (black points on the plot, each representing a randomly chosen field of view), which is used to calculate the force per fiber as a function of strain from the total force applied to the sample. Inset images are 4 μm across. At least 10 scanning and transmission electron microscope images at each strain were obtained from two independently prepared samples with similar results.

in fibrinogen oligomers (*17*). A more gradual unfolding has been observed in molecular dynamics simulations (*21*), but the coiled-coil spanning αC region is missing from published crystal structures of fibrinogen and is therefore not included in the simulation. Early wide-angle x-ray scattering measurements of fibrin clots support this view of molecular extension (*22*), providing evidence for a folding transition from α helix to β sheet, as has been observed for stretched keratin (*23*, *24*).

When these results are taken together, the following picture of fibrin mechanics emerges (Fig. 1). Because fibrin fibers are straight and relatively stiff, thermally induced bends are negligible, and so there is no slack to be pulled out upon extension. Instead, even at relatively low strains, the fibers themselves must begin to orient and stretch along the direction of the applied strain. The volume fraction of protein within the fibers has been estimated at ~20% (*25*), and the protofibrils that make up the fibers are known to adopt a twisted conformation (*26*) so that, at low strains, fibers could stretch somewhat by having protofibrils straighten and untwist within the fibers. However, to reach even a strain of ~0.15, unfolding must start to play a role. It is this structural transition that allows fibrin clots to maintain their linear response until strains of 1.2, at which point the coiled coils, or perhaps some other compact structures, are stretched to near their unfolded contour lengths, leading to strain hardening. The unfolded domains then interact and expel water, as many denatured proteins do.

To quantitatively test this mechanism, two approaches to model the stress-strain behavior of networks of semi-flexible filaments can be adapted for fibrin. A first model for random networks of folded proteins (*27*) uses a system of connected fibers. Although this model is not explicitly based on the microscopic structure of the network, it has been shown to accurately describe other random networks and serves to connect the microscopic and macroscopic processes. This leads to an expression for the force-extension (or stress-strain) relation of the network in terms of the force-extension relation of a single fiber. The molecules making up the fiber are modeled as two-state systems that can be either folded, in which case the fiber behaves as a linear spring, or unfolded, in which case it is modeled as a wormlike chain (*28*) (see SOM).

An alternative model of filamentous gels starts from the assumption that the networks are homogeneous and isotropic, and strain uniformly (*29*). Such a model can be used to compute the mechanical properties of the network after choosing a fiber force-extension curve as above. This model captures the trend in the data if buckling is taken into account by setting the force on a fiber to zero whenever it is under compression.

With either modeling approach, protein unfolding is required to fit the experimental data. Without unfolding, the fit rapidly diverges from the experimental force-extension curve (Fig. 2A, black dashed line). The fraction of folded domains n_f determined from the model correlates with the decreasing Scherrer length L observed with SAXS (Fig. 4D), providing further evidence that sample disordering is due to molecular extension. The divergence at high strains is probably due to unfolding of structures in the fibrin molecules other than coiled coils, which has been suggested as a possible mechanism to account for the extensibility of single fibrin fibers (*11*) and could be straightforwardly incorporated into our model to fit the force-extension data at the highest strains. In contrast, a linear model without unfolding fits collagen force extension data reasonably well (see SOM). This further highlights the uniqueness of fibrin's ability to balance large extensibility with a large pore size.

To account for the measured volume change in addition to the other results, we modified the first model (*27*) by associating a volume decrease with the unfolding transition. By matching the volume change at high strain, we determined the fractional volume change per domain and then, with no further fitting, the observed volume drop at low strain was captured using the same parameters as those used to fit the force-extension curve (compare Figs. 2B and 4D). The approximate fit to the negative peak in the compressibility (Fig. 2B, inset) further increases confidence in the model and again suggests a connection between clot shrinkage and an unfolding transition (SOM Eq. 29). A likely mechanism is aggregation that buries hydrophobic residues exposed during forced unfolding of protein (fig. S3).

Thus, it is the molecular extensibility of fibrin that allows clots' long straight fibers to extend and that endows them with essential properties, such as large pore sizes and low fibrin volume fraction in combination with extensibility. This allows for efficient permeation and lysis of clots (*5*) and maintenance of mechanical integrity in dynamic environments (e.g., platelet-induced clot retraction, skin and internal wounds that could stretch during healing, arterial thrombi, and pulsatory thrombotic aneurysms). The fact that these molecular transitions occur at small strains that cells can exert (*30*) and are manifested directly in the macroscopic mechanics of fibrin may represent a clear example of an important biological function of forced protein unfolding, as also

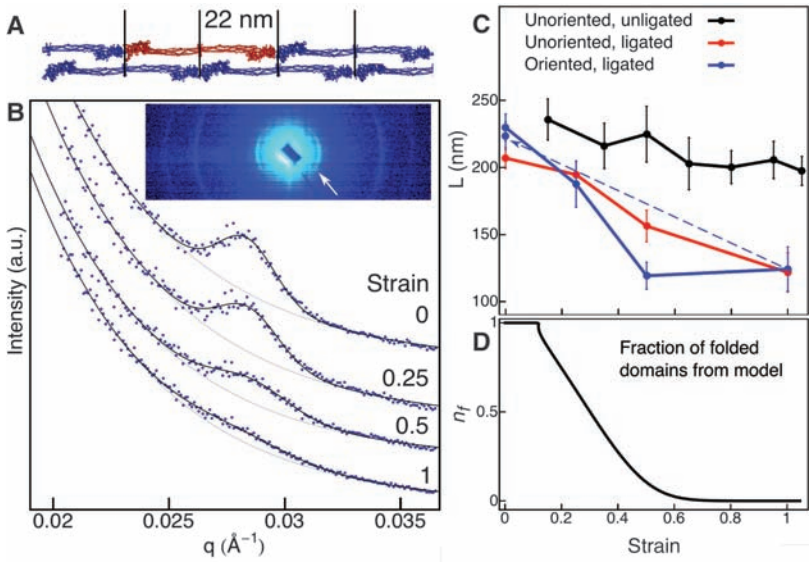

Fig. 4. Structural changes in stretched fibrin clots at the molecular level. (**A**) Schematic of a fibrin protofibril showing the half-staggered pattern that leads to a characteristic 22-nm repeat. A fibrin monomer within the protofibril is shown in red. (**B**) SAXS from fibrin clots leads to a clear first-order peak (white arrow, inset) and to third- and fourth-order peaks. The plots show the peak shape as a function of the wave vector $q = 2\pi/d$, which increases radially from the center (here, d is the fibrin periodicity, 22 nm). The thick lines are fits to the data using the sum of an exponential and a Gaussian with the exponential alone (thin lines) shown for comparison. The width of the peak increases with increasing stretch, which can be understood in terms of a two-state–like extension of fibrin molecules that introduce defects into the sample. a.u., arbitrary units. (**C**) This effect is quantified as the Scherrer length L, which decreases with increasing strain (red). The decrease is more rapid for samples that were prealigned in a magnetic field during polymerization (blue), which implies that network alignment accommodates some strain and delays unfolding. The transition is reversible when samples are allowed to relax, as indicated by the blue arrow. When samples are not ligated using factor XIIIa, protofibril sliding becomes important, and unfolding is decreased. In all cases, the peak position remains relatively constant, implying that there is no gradual lengthening of the whole population of fibrin monomers. Instead, there remains a population that is not unfolded and maintains a fairly constant spacing. Error bars indicate SDs of the distribution of L determined from fits using the bootstrap method. This bootstrap error is similar to the average SE of 15 nm calculated by averaging over results from four samples. (**D**) This behavior is captured by the constitutive model in which the fraction of folded monomers n_f decreases with increasing strain.

demonstrated for some proteins in stressed cells (*31*). Unfolded domains could be promising targets for modification in applications such as tissue engineering and cell biophysics, where stiffness is known to be important (*30*), and for designs of tougher fibrin sealants used in surgeries (*32*). Controlling unfolding could also lead to new strategies for breaking thrombi, perhaps by stabilizing the coiled coil, rendering clots more brittle for thrombectomy, or by destabilizing the coiled coil, making clots softer and less occlusive. Structural transitions observable at multiple scales may also be involved in the mechanics of other protein assemblies.

References and Notes

1. J. W. Weisel, in *Advances in Protein Chemistry*, vol. 70 (Academic Press, London, 2005), pp. 247–299.
2. N. Laurens, P. Koolwijk, M. P. M. DeMaat, *J. Thromb. Haemost.* **4**, 932 (2006).
3. R. W. Colman *et al.*, *Hemostasis and Thrombosis: Basic Principles and Clinical Practice* (Lippincott Williams & Wilkins, Philadelphia, 2005).
4. J. W. Weisel, *Biophys. Chem.* **112**, 267 (2004).
5. J. P. Collet *et al.*, *Arterioscler. Thromb. Vasc. Biol.* **20**, 1354 (2000).
6. D. A. Gabriel, K. Muga, E. M. Boothroyd, *J. Biol. Chem.* **267**, 24259 (1992).
7. B. A. Roeder *et al.*, *J. Biomech. Eng.* **124**, 214 (2002).
8. Materials and methods are available as supporting material on *Science* Online.
9. P. A. Janmey, E. J. Amis, J. D. Ferry, *J. Rheol.* **27**, 135 (1983).
10. The clots typically break where they are clamped, suggesting that the true clot extensibility is larger than that measured here.
11. W. Liu *et al.*, *Science* **313**, 634 (2006).
12. L. R. G. Treloar, *The Physics of Rubber Elasticity* (Clarendon, Oxford, 1975).
13. D. P. Kharakoz, *Biophys. J.* **79**, 511 (2000).
14. H. Kang *et al.*, *J. Phys. Chem. B* **113**, 3799 (2009).
15. The orientational order parameter is defined as $\langle \cos 2\theta \rangle$, where θ is the angle of the fiber determined at each fiber pixel (see SOM for a description of the analysis algorithm).
16. M. F. Müller, H. Ris, J. D. Ferry, *J. Mol. Biol.* **174**, 369 (1984).
17. A. E. X. Brown, R. I. Litvinov, D. E. Discher, J. W. Weisel, *Biophys. J.* **92**, L39 (2007).
18. L. Stryer, C. Cohen, R. Langridge, *Nature* **197**, 793 (1963).
19. F. J. Roska, J. D. Ferry, J. S. Lin, J. W. Anderegg, *Biopolymers* **21**, 1833 (1982).
20. L. E. Alexander, *X-Ray Diffraction Methods in Polymer Science* (Wiley, Hoboken, NJ, 1979).
21. B. B. C. Lim, E. H. Lee, M. Sotomayor, K. Schulten, *Structure* **16**, 449 (2008).
22. K. Bailey, W. T. Astbury, K. M. Rudall, *Nature* **151**, 716 (1943).
23. W. T. Astbury, H. J. Woods, *Proc. R. Soc. London Ser. B Biol. Sci.* **114**, 314 (1934).
24. J. W. S. Hearle, *Int. J. Biol. Macromol.* **27**, 123 (2000).
25. W. A. Voter, C. Lucaveche, H. P. Erickson, *Biopolymers* **25**, 2375 (1986).
26. J. W. Weisel, C. Nagaswami, L. Makowski, *Proc. Natl. Acad. Sci. U.S.A.* **84**, 8991 (1987).
27. H. J. Qi, C. Ortiz, M. C. Boyce, *J. Eng. Mater. Technol.* **128**, 509 (2006).
28. C. Bustamante, J. F. Marko, E. D. Siggia, S. Smith, *Science* **265**, 1599 (1994).
29. C. Storm *et al.*, *Nature* **435**, 191 (2005).
30. D. E. Discher, P. Janmey, Y.-l. Wang, *Science* **310**, 1139 (2005).
31. C. P. Johnson, H.-Y. Tang, C. Carag, D. W. Speicher, D. E. Discher, *Science* **317**, 663 (2007).
32. D. M. Albala, *Cardiovasc. Surg.* **11**, 5 (2003).

33. We thank P. Heiney for help with the x-ray diffraction measurements (NSF–Materials Research Science and Engineering Center partial support); C. Nagaswami for scanning electron microscopy; D. Galanakis for his gift of fibrinogen; S. Pickup for access to the magnet facility; A. Kota for help with the tensile testing; J. Torbet for discussions of x-ray diffraction and magnetic alignment; and P. Janmey, T. Lubensky, H. Shuman, and C. Storm for useful discussions. This work was supported by NIH (grants HL090774 and HL30954 to J.W.W. and grant HL62352 to D.E.D.) and by the Nano/Bio Interface Center through NSF Nanoscale Science and Engineering Center (grant DMR-0425780). A.E.X.B. was supported by a scholarship from the Natural Sciences and Engineering Research Council of Canada.

Supporting Online Material

www.sciencemag.org/cgi/content/full/325/5941/741/DC1
Materials and Methods
SOM Text
Figs. S1 to S11
References
Movie S1

18 February 2009; accepted 19 June 2009
10.1126/science.1172484

The C-Ala Domain Brings Together Editing and Aminoacylation Functions on One tRNA

Min Guo, Yeeting E. Chong, Kirk Beebe,* Ryan Shapiro, Xiang-Lei Yang, Paul Schimmel†

Protein synthesis involves the accurate attachment of amino acids to their matching transfer RNA (tRNA) molecules. Mistranslating the amino acids serine or glycine for alanine is prevented by the function of independent but collaborative aminoacylation and editing domains of alanyl-tRNA synthetases (AlaRSs). We show that the C-Ala domain plays a key role in AlaRS function. The C-Ala domain is universally tethered to the editing domain both in AlaRS and in many homologous free-standing editing proteins. Crystal structure and functional analyses showed that C-Ala forms an ancient single-stranded nucleic acid binding motif that promotes cooperative binding of both aminoacylation and editing domains to $tRNA^{Ala}$. In addition, C-Ala may have played an essential role in the evolution of AlaRSs by coupling aminoacylation to editing to prevent mistranslation.

The algorithm of the genetic code is established in the first reaction of protein synthesis. In this reaction, aminoacyl–transfer RNA (tRNA) synthetases (AARSs) catalyze the attachment of amino acids to their cognate tRNAs that bear the triplet anticodons of the genetic code. When a tRNA is acylated with the wrong amino acid, mistranslation occurs if the misacylated tRNA is released from the synthetase, captured by elongation factor, and used at the ribosome for peptide synthesis. To prevent mistranslation, some AARSs have separate editing activities that hydrolyze the misacylated amino acid from the tRNA (*1*–*3*). Because an editing-defective tRNA synthetase is toxic to bacterial and mammalian cells (*4*, *5*) and is causally linked to disease in animals (*6*), strong selective pressure retains these editing activities throughout evolution.

A particular challenge appears to be avoiding mistranslation of serine or glycine for alanine. All three kingdoms of life contain free-standing editing-proficient homologs of the editing domains found in alanyl-tRNA synthetases (AlaRSs) (*7*). These proteins, known as AlaXps, provide functional redundancy by capturing mischarged $tRNA^{Ala}$ molecules that escape the embedded editing activities of AlaRSs (*8*). Although free-standing editing domains have counterparts in ThrRS and ProRS (*7*, *9*, *10*), they are not as evolutionarily conserved as AlaXps. Moreover, enzymes like LeuRS, IleRS, and ValRS lack any free-standing editing domain counterparts (*1*, *2*, *11*, *12*). Despite the multiple checkpoints to prevent mischarging of $tRNA^{Ala}$, we did not know how the apparatus for preventing confusion of serine and glycine for alanine was assembled. To pursue this question, we focused on a third domain separate from the editing and aminoacylation domains, known as C-Ala, which is found in all AlaRSs and is tethered to their editing domains.

The modular arrangement of domains in AlaRSs is evolutionarily conserved (*13*) (Fig. 1A). The N-terminal aminoacylation domain is active as an isolated fragment, and its three-dimensional structure is that of a typical class II AARS. The central editing domain is homologous to the editing domain of the class II ThrRS (*14*, *15*). Lastly, a linker tethers the third (C-Ala) domain to the editing domain. In contrast to the other two domains, C-Ala is only loosely conserved and its structure is unknown. On the basis of a survey of AlaRS sequences, we predicted that a fragment corresponding to residues 766 to 875 of *Escherichia coli* AlaRS would form a structural unit (Fig. 1B). The corresponding region of *Aquifex aeolicus* AlaRS is the 110–amino acid fragment encompassing residues 758 to 867, which was expressed in *E. coli*, purified, and crystallized (*16*). The structure was solved to a resolution of 1.85 Å

The Skaggs Institute for Chemical Biology and the Department of Molecular Biology, The Scripps Research Institute, BCC-379, 10550 North Torrey Pines Road, La Jolla, CA 92037, USA.

*Present address: Metabolon, Incorporated, 800 Capitola Drive, Suite 1, Durham, NC 27713, USA.

†To whom correspondence should be addressed. E-mail: schimmel@scripps.edu

Supporting Online Material for

Multiscale Mechanics of Fibrin Polymer: Gel Stretching with Protein Unfolding and Loss of Water

André E. X. Brown, Rustem I. Litvinov, Dennis E. Discher, Prashant K. Purohit, John W. Weisel*

*To whom correspondence should be addressed. E-mail: weisel@mail.med.upenn.edu

Published 7 August 2009, *Science* **325**, 741 (2009)
DOI: 10.1126/science.1172484

This PDF file includes:

Other Supporting Online Material for this manuscript includes the following: (available at www.sciencemag.org/cgi/content/full/325/5941/741/DC1)

Supporting Online Material

This document includes:

Materials and Methods

Preparation of Fibrin and Cylindrical Clots
To form a fibrin clot, 10 mg/ml purified human fibrinogen in 50 mM Tris-HCl buffer, pH 7.4, containing 150 mM NaCl, 10 mM $CaCl_2$, and 10 μg/ml human Factor XIII, was mixed with 0.5 U/ml (final concentration) human thrombin. Cylindrical clots were prepared in a 4x60 mm or a 2x50 mm plastic tube whose barrel was lubricated with a very thin layer of 25% (v/v) Triton X-100 to minimize sticking of the clot to the walls. The clots were allowed to form for 3-5 hours at room temperature and then kept overnight at 4°C. To form a magnetically oriented clot, immediately after the addition of thrombin the plastic tubes were placed for 3-5 hours in a 9.4T bore magnet, so that the vector of the magnetic field was collinear with the tube axis. Then, these clots were slipped out of the tube and used for experiments. Covalent ligation of the clots by Factor XIIIa was corroborated by the presence of the γ-γ-chain band and α-chain polymers in SDS-PAGE of reduced samples of the clot preparation.

Tensile Testing
Cylindrical clots were gently clamped between rubber pads in the grips of a strain-controlled Instron tensile tester equipped with a 2.5 N load cell. Samples were stretched at 10 mm per minute while monitoring the load. To determine the strain in the center of the sample independent of any effects of clamping, graphite powder was used to make fiducial marks on the clots that were then imaged using a digital camera. NIH ImageJ was used to track the size and location of the fiducial marks in the center of the sample over the course of the stretching experiments and these marks were used to calculate the longitudinal strain and λ_*, the relative change in diameter. Fig. S1 shows a clot before and after stretching with yellow dots indicating the points chosen to determine the strain and diameter. In this way, the strain in the center of the sample was determined to eliminate any effects due to the compliance of the clamping points at the sample ends. Clots stretched in air and in a bath containing buffer (50 mM Tris-HCl, pH 7.4, 150 mM NaCl, 3 mM $CaCl_2$) showed similar extensibility and volume decrease indicating that even the clots that were exposed to air during the test remained hydrated. The extensibility results are reported as mean ± standard error.

Measuring Protein Content in Clots
To measure protein content in a fibrin clot, a piece of unstretched or stretched 2-mm cylindrical clot was gently blotted, weighed, and dissolved in 0.1M NaOH. Then the protein concentration was measured by spectrophotometer at a wavelength of 280 nm and the absorbance was normalized by the total mass of the piece of the clot. An increase in protein content in a fibrin clot is inversely proportional to the clot shrinkage upon stretching.

Scanning Electron Microscopy
Clots prepared for scanning electron microscopy were thoroughly washed by permeation with 50 mM sodium cacodylate-HCl buffer, pH 7.4, to remove excess salt and fixed overnight in 2% glutaraldehyde. Stretched clots were washed and fixed by immersion into the buffer or fixative while being clamped in the stretching device right after they reached a certain length. Clots then were cut into small pieces, washed in DI water, dehydrated in a graded series of increasing ethanol concentrations (30-100%), and critical point dried with CO_2 in a DCP-1 Critical Point Drying Apparatus (Denton Vacuum Co., Cherry Hill, NJ). The specimens were mounted, sputter coated with gold-palladium in a Sputter Coating Unit E5100 (Polaron Instruments, Inc.) at 2.2 kV and 20 mA for 1.5 min, and examined in an FEI XL20 scanning electron microscope (FEI Co., Hillsboro, OR). Duplicates of each clot were made, and several fields on each clot were examined before choosing fields that are characteristic of the entire clot. Digital electron micrographs were taken at different magnifications between 2,000x and 10,000x.

Transmission Electron Microscopy of Transverse Sections
Cylindrical clot samples were fixed in 2.0% glutaraldehyde in 0.1M sodium cacodylate buffer, pH 7.4, overnight. After post fixation with 2% osmium tetroxide, the samples were stained en bloc with 2% uranyl acetate, dehydrated through a graded ethanol series, and embedded in PolyBed 812 (Polysciences Inc.). Thin transverse sections were stained with uranyl acetate and bismuth subnitrite and examined with a JEOL 1010 electron microscope fitted with a Hamamatsu digital camera and AMT imaging software.

Image Analysis
Scanning electron micrographs were segmented and analyzed using the following procedure that was implemented in Mathematica (Wolfram Research Inc., Champagne, IL). A series of elongated Laplace of Gaussian (eLoG) filters at different orientations were generated by convolving elongated Gaussian kernels (i.e. two-dimensional Gaussians with a larger standard deviation in one direction than in the orthogonal direction) with an approximation of a Laplacian. Images were convolved with the eLoG filters at each orientation generating a series of filtered images. A maximum response image was constructed by taking the maximum over the filtered images at each pixel. The inset images shown in Fig. 3B are thresholded versions of the maximum response images that have been color-coded according to the orientation of the eLoG that gave the maximum response at each pixel. The orientation of the eLoG that gave the maximum response is defined as that pixel's orientation and it is the distribution of these pixel orientations that is used to calculate the orientational order parameter as $\langle \cos(2\theta) \rangle$, where the average is over the orientation distribution.

Small Angle X-ray Scattering (SAXS)

Samples were clamped in a custom built chamber to prevent them from being exposed to the vacuum of the X-ray apparatus and drying. The chamber consists of a box with one removable face, sealed with a rubber o-ring. Inside the box is a linear device for strain adjustment with metal clips to hold the clots. Rubber pads are used to protect the clots from the metal clips. Beryllium windows are stuck into rectangular holes in the faces of the box using vacuum resistant epoxy to allow X-rays to pass into and out of the chamber. The SAXS apparatus uses a Bruker Nonius FR591 rotating-anode X-ray generator, doubly-focusing mirror-monochromator optics, and a Bruker Hi-Star multiwire detector. Before each experiment the instrument was calibrated using a silver behenate standard. Data analysis was performed using Datasqueeze 2.1 (http://www.datasqueezesoftware.com/).

These SAXS measurements on fibrin yield a ~22 nm repeat. Although earlier measurements on fibrin films suggested that this spacing increased with stretching [1], the lower resolution and signal to noise ratio in these data make peak assignment difficult. Furthermore, the preparation of the fibrin films involved substantial long-term compression, so these conclusions do not apply directly to fully hydrated networks as studied here.

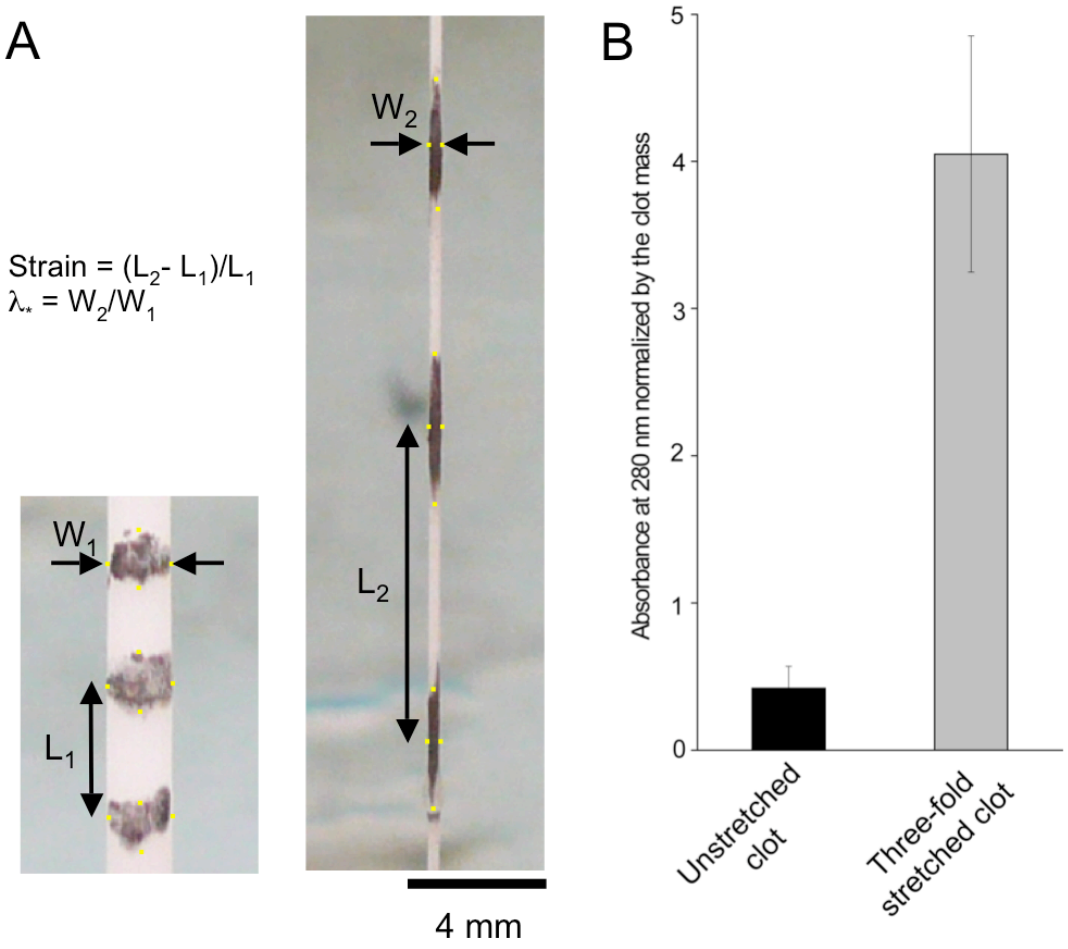

Fig. S1: Determining dimensions (on the left) and protein content (on the right) of unstretched vs. stretched clots. The boundaries of the fiducial marks are determined manually in NIH ImageJ for each image taken during the tensile test (yellow marks). The longitudinal strain is calculated from the distance between the centers of two fiducial marks. The centers are defined as the average vertical position of the top and bottom yellow dots. Changes in sample width are determined from the manually determined lateral dimensions. Protein content in unstretched and stretched clots was determined as described in materials and methods.

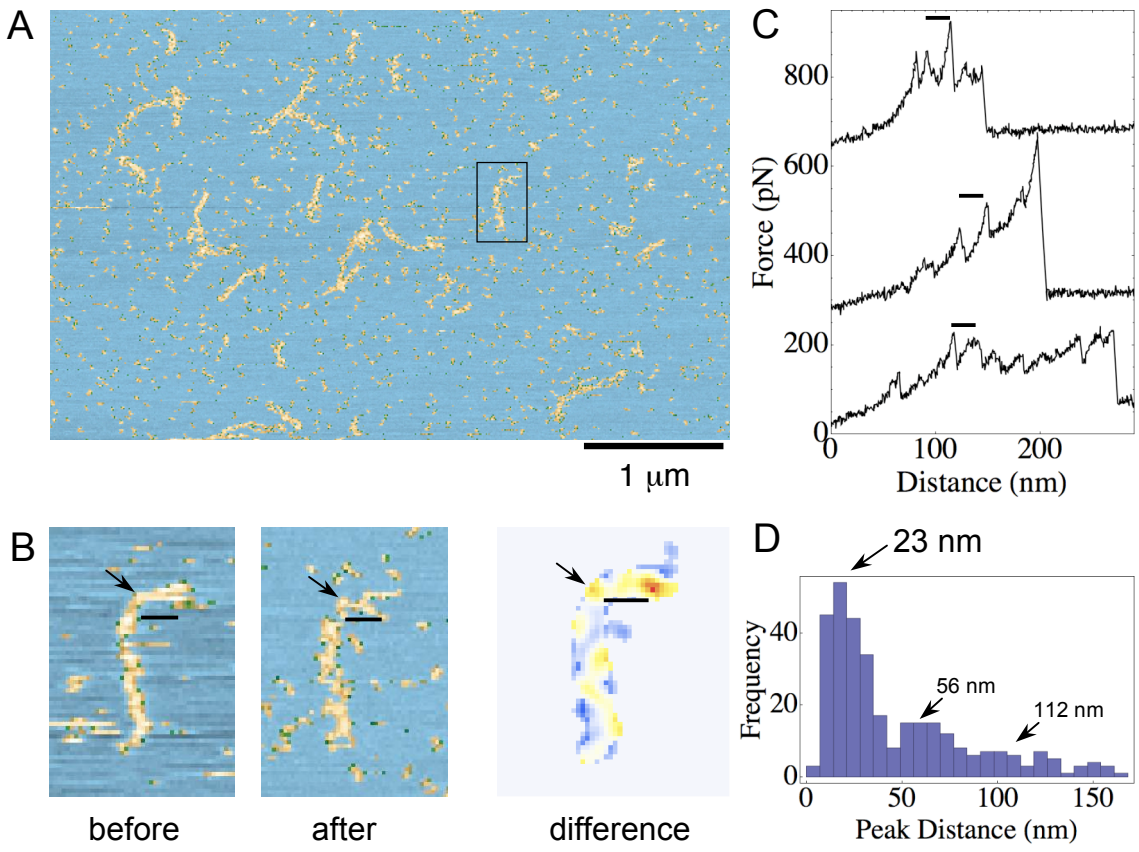

Fig. S2: Forced unfolding of single protofibrils by atomic force microscopy (AFM) using an image-pull-image protocol. **(A)** AFM height image of fibrin protofibrils adsorbed on a mica surface in buffer. **(B)** An expanded view of the protofibril marked by the black box in (A) that was probed in force-mode at the location shown by the black arrow. Several force curves were recorded between the before and after images with a typical extended length of 200 nm, which is indicated by the small scale bars in each image. After smoothing and zeroing the background, the images were subtracted to generate the difference image shown at the right. Given the large size of the protofibrils compared to structures that are normally pulled using AFM, these measurements push the limits of what is possible using non-specific adsorption to attach the tip to the sample and this is reflected by the relatively small difference between the before and after images. Nonetheless, there is a larger difference at the end of the extended region in the top-right part of the image and the corresponding force-extension curves **(C)** show a characteristic repeat of around 23 nm. This is the distance expected for coiled-coil unfolding, as observed previously for simpler end-to-end oligomers. **(D)** Histogram of peak-to-peak distances observed in several force curves with a peak around 23 nm. Thus, the more complex interactions in protofibrils do not affect the previously observed result that the coiled-coils unfold before the other fibrin domains under force and that this unfolding occurs in an all-or-nothing manner.

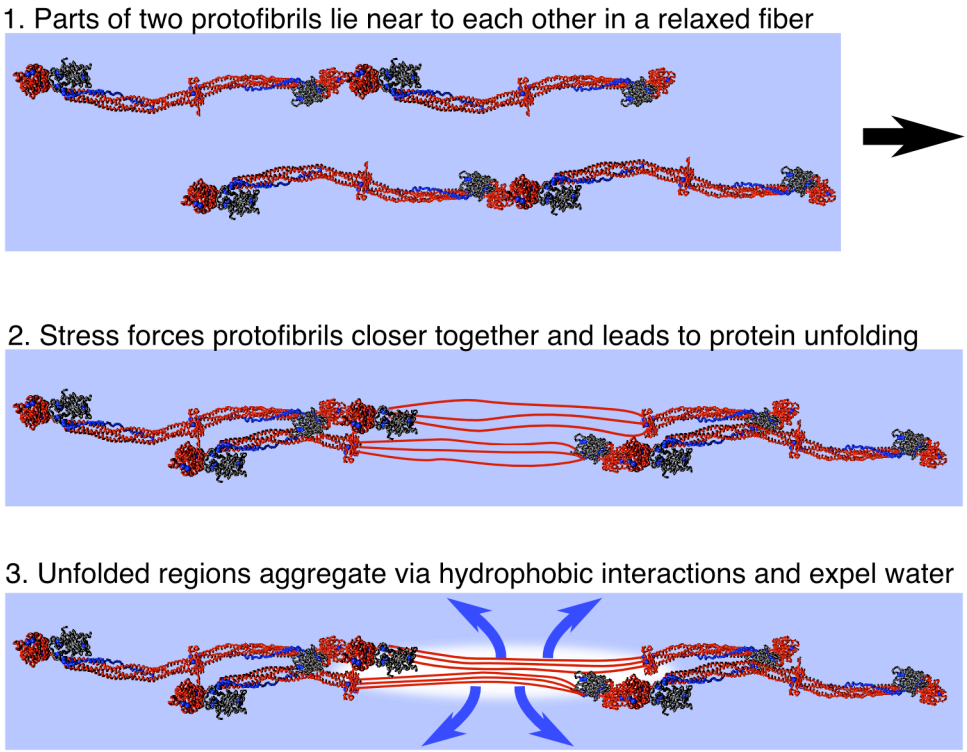

Fig. S3: Schematic of proposed mechanism of volume decrease and water expulsion. Partial segments of two adjacent protofibrils are depicted with the surrounding water shown in blue. Hydrophobic side chains are exposed during unfolding and aggregate.

Modeling of fibrin mechanics

In this section we describe three different methods to obtain the constitutive relation for a network of fibrin fibers. The first method is based on the eight-chain model of Qi *et al.* [2] (see Fig. S4(b)), the second, on the three-chain model [3] which is an older version of the eight-chain model (see Fig. S4(a)), and the third is based on the isotropic network model of Storm *et al.* [4]. All these methods were developed to describe the behavior of random isotropic networks of fibers, such as elastomers and biological gels, all assume affine deformations, and all consider the networks as being incompressible. These methods have been successfully applied to many biological and non-biological polymers with widely different structures. Thus, it is appropriate to apply them to the fibrin clot, which is an isotropic network of branched fibers, typically with three fibers joined at each branch point (Fig. S5).

These network models have a long history[1] dating back to the 1940s when it was recognized that the elasticity of rubber has its origins in the changing configurational entropy of stretched chains. In particular, it was found that the response of an isotropic network of n randomly oriented chains per unit volume is identical to that of $n/3$ single chains in three orthogonal directions (three-chain model, see Fig. S4(a)). The three-chain model was in widespread use until the early 1990s when Arruda and Boyce found that this model was unable to capture the deformation dependence of strain-hardening in some polymers. Arruda and Boyce [6] then proposed the eight-chain model which gave much better agreement with experiments and has since been used to interpret experiments on biopolymer networks. The isotropic network model of Storm *et al.* has also been used to interpret experiments on biopolymer networks and relies on a knowledge of the spatial distribution of chain orientations as in Wu and van der Giessen [5] and numerous other earlier works. A detailed study comparing these three models has determined that approximations based on the three- and eight-chain models agree very well with the predictions of the isotropic network model over the entire range of strains [5].

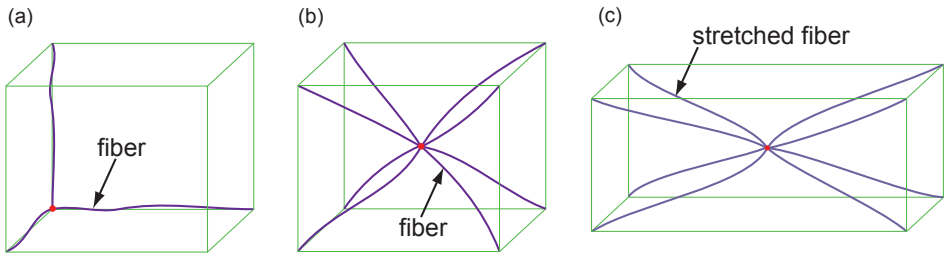

Fig. S 4: Models for isotropic networks. (a) In the three-chain model three chains are aligned along the sides of a cube. The strain energy stored in the chains upon deformation can be used to calculate the strain-energy density of the deformed cube. (b) In the eight-chain model eight chains connect the vertices of cube to the body center. The strain energy density of the cube is computed in a similar way. Note that the geometry of the models need not correspond to the actual geometry of the networks. (c) An eight-chain cube in a deformed state in which there is stretching in the longitudinal direction and contraction along the other two orthogonal directions.

[1] An excellent account of the course of development of these models can be found in Wu and van der Giessen [5].

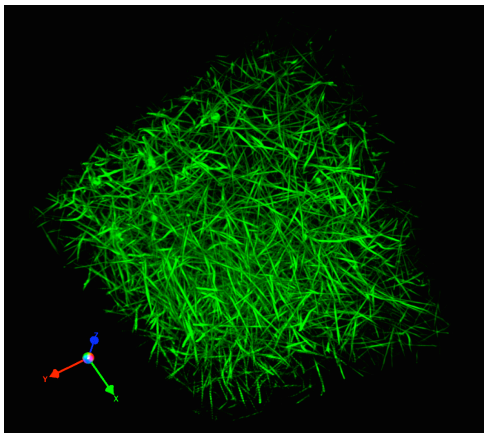

Fig. S 5: A three-dimensional reconstruction of a hydrated fibrin network obtained using fluorescent confocal microscopy by A. Stout, K. Gersh, and J. Weisel (Dept. of Cell and Developmental Biology, School of Medicine, University of Pennsylvania, Philadelphia.).

The model of Qi *et al.* [2] connects the microscopic mechanics of the fibers to the macroscopic behavior of the network by constructing a cube each of whose eight vertices is connected to the body center through a fiber (see Fig. S4(b)). For a given state of strain the strain energy density of this cube is assumed to be equal to the strain energy density of the network. But, the strain energy density of the cube can be explicitly written in terms of the energy stored in the eight deformed fibers allowing us to connect the macroscopic network parameters to the microscopic behavior of the fibers. The strain-energy density in the three-chain model is evaluated along similar lines except that the fibers are oriented along three perpendicular directions (see Fig. S4(b)). These models are not based on the microscopic structure of the network. However, the eight-chain model has been shown to accurately describe other random networks [7], such as, those of actin filaments and rubbers. On the other hand, the isotropic network model of Storm *et al.* [4] is more physically realistic and is motivated by the observation that fibers in an isotropic network are equally likely to be oriented along any direction. Therefore, Storm *et al.* [4] connect the network stress-strain behavior to the fiber force-extension relation by integrating over all possible fiber orientations. However, an important advantage of the three- and eight-chain models is that they provide analytical expressions that can be fitted to the experimental data, where as, the isotropic network model can only be implemented computationally.

An important feature of fibrin networks is that their deformation is accompanied by significant changes in volume. None of the models mentioned above accounts for these effects. It is straight forward to modify the eight-chain model and three-chain model to account for volume changes, but it is not immediately apparent how to do so in isotropic network model of Storm *et al.* [4]. In the following we describe all these methods and show how we can use them to interpret experimental data.

Eight-chain model

As a model for a random network we first describe the eight chain cube of Qi *et al.* [2]. Each chain or fiber extends from the center of the cube to one of its vertices. The reference (undeformed)

length of each fiber is L and the side of the undeformed cube is a, so that $L = \frac{\sqrt{3}}{2}a$. The cube suffers large deformations in response to an applied stress. After deformation, the sides of the cube are uniformly stretched by λ_1, λ_2 and λ_3. Hence, the length of each fiber after deformation is $\lambda_c L$ where

$$3\lambda_c^2 = \lambda_1^2 + \lambda_2^2 + \lambda_3^2. \tag{1}$$

Let the strain-energy stored in each fiber due to the deformation be $G(\lambda_c)L$ where $G(\lambda_c)$ is the strain energy per unit reference length of the fiber. Then the force-extension relation of the fiber is given by

$$F(\lambda_c) = \frac{dG}{d\lambda_c}. \tag{2}$$

The contribution to the strain energy per unit reference volume due to the deformation of the fibers is given by

$$U_1 = \nu L G(\lambda_c), \tag{3}$$

where $\nu = \frac{3\sqrt{3}}{L^3}$ is the number of fibers per unit reference volume. The volume of the cube changes after deformation. If V is the reference volume and ΔV is the deformed volume then $\frac{\Delta V}{V} = \lambda_1\lambda_2\lambda_3 - 1$. Let $U_2 = g(\lambda_1\lambda_2\lambda_3)$ be the contribution to the strain energy per unit reference volume due to volume changes. Then the total strain energy per unit reference volume of a network consisting of these eight chain cubes is given by

$$U = U_1 + U_2 = \nu L G(\lambda_c) + g(\lambda_1\lambda_2\lambda_3). \tag{4}$$

Similar expressions for the network strain energy density were given by Flory [8] and others. [2]

Now, let $\mathbf{F} = \frac{\partial \mathbf{y}}{\partial \mathbf{x}}$ be the deformation gradient tensor, where $\mathbf{y}$ is the deformed position of a particle whose reference position is $\mathbf{x}$. Then the right Cauchy-Green strain tensor is defined as $\mathbf{C} = \mathbf{F}^T\mathbf{F}$. If we work in principal co-ordinates then it is easy to see that

$$C_{11} = \lambda_1^2, \qquad C_{22} = \lambda_2^2, \qquad C_{33} = \lambda_3^2, \qquad C_{12} = C_{13} = C_{23} = 0. \tag{5}$$

From the principles of continuum mechanics it is known that the second Piola-Kirchhoff stress tensor $\mathbf{S}$ (applied force mapped to the reference configuration divided by the reference area) is work conjugate to the right Cauchy-Green strain tensor $\mathbf{C}$ [2]. In other words,

$$S_{11} = \frac{\partial U}{\partial C_{11}}, \qquad S_{22} = \frac{\partial U}{\partial C_{22}}, \qquad S_{33} = \frac{\partial U}{\partial C_{33}}. \tag{6}$$

The shear stresses are zero since we are working in principal co-ordinates and assuming that the network is isotropic due to randomness. By the use of the chain rule we find that

$$S_{11} \;=\; \frac{\nu L F(\lambda_c)}{6\lambda_c} + \frac{\lambda_1\lambda_2\lambda_3}{2\lambda_1^2} f(\lambda_1\lambda_2\lambda_3), \tag{7}$$

[2] According to Flory [8] $U = \frac{\mu}{2}(3\lambda_c^2 - 3) - \mu \log(\lambda_1\lambda_2\lambda_3)$, where μ is the network shear modulus for small strains. The shear modulus for the eight-chain cube along the 110 and symmetry related directions can be computed by calculating the network strain energy density for a pure shear given by $\lambda_1 = \lambda$, $\lambda_2 = \lambda^{-1}$, $\lambda_3 = 1$. The detailed calculation was performed by Arruda and Boyce [6] who showed that the strain energy density U can be written as a series in powers of $(\lambda_c^2 - 3)$. Taking $\lambda = 1 + \gamma$ where $\gamma << 1$, the lowest order term in this series is proportional to γ^2. This suggests a finite shear modulus for the eight-chain cube along the 110 and symmetry related directions.

$$S_{22} = \frac{\nu LF(\lambda_c)}{6\lambda_c} + \frac{\lambda_1\lambda_2\lambda_3}{2\lambda_2^2} f(\lambda_1\lambda_2\lambda_3), \tag{8}$$

$$S_{33} = \frac{\nu LF(\lambda_c)}{6\lambda_c} + \frac{\lambda_1\lambda_2\lambda_3}{2\lambda_3^2} f(\lambda_1\lambda_2\lambda_3), \tag{9}$$

where $f(p) = g'(p)$. The Cauchy stress σ (applied force in the deformed configuration divided by area in the deformed configuration) is given by $\sigma = \frac{1}{det(\mathbf{F})}\mathbf{FSF}^T$. Hence, the components of the Cauchy stress are:

$$\sigma_{11} = \frac{\lambda_1^2}{\lambda_1\lambda_2\lambda_3} S_{11} = \frac{\lambda_1^2}{\lambda_1\lambda_2\lambda_3} \frac{\nu LF(\lambda_c)}{6\lambda_c} + \frac{1}{2} f(\lambda_1\lambda_2\lambda_3), \tag{10}$$

$$\sigma_{22} = \frac{\lambda_2^2}{\lambda_1\lambda_2\lambda_3} S_{22} = \frac{\lambda_2^2}{\lambda_1\lambda_2\lambda_3} \frac{\nu LF(\lambda_c)}{6\lambda_c} + \frac{1}{2} f(\lambda_1\lambda_2\lambda_3), \tag{11}$$

$$\sigma_{33} = \frac{\lambda_3^2}{\lambda_1\lambda_2\lambda_3} S_{33} = \frac{\lambda_3^2}{\lambda_1\lambda_2\lambda_3} \frac{\nu LF(\lambda_c)}{6\lambda_c} + \frac{1}{2} f(\lambda_1\lambda_2\lambda_3), \tag{12}$$

$$\sigma_{12} = \sigma_{13} = \sigma_{23} = 0. \tag{13}$$

At this point we consider a uniaxial tension test on a cylindrical specimen. The force f_{ap} is applied along the $\mathbf{e}_1$ direction. We therefore set $\sigma_{22} = \sigma_{33} = 0$ and $\lambda_2 = \lambda_3 = \lambda_*$ in the expressions above. This immediately shows that

$$\frac{1}{2} f(\lambda_1\lambda_*^2) = -\frac{1}{\lambda_1} \frac{\nu LF(\lambda_c)}{6\lambda_c}, \tag{14}$$

and,

$$\sigma_{11} = \left(\frac{\lambda_1}{\lambda_*^2} - \frac{1}{\lambda_1}\right) \frac{\nu LF(\lambda_c)}{6\lambda_c} \tag{15}$$

If the radius of the cylinder in the reference configuration is R_0 then its deformed radius is $\lambda_* R_0$ and the applied force is given by

$$f_{ap} = \pi\lambda_*^2 R_0^2 \sigma_{11} = \left(\lambda_1 - \frac{\lambda_*^2}{\lambda_1}\right) \frac{\pi R_0^2 \nu LF(\lambda_c)}{6\lambda_c}, \qquad \lambda_c = \sqrt{\frac{\lambda_1^2 + 2\lambda_*^2}{3}}. \tag{16}$$

In an experiment λ_1 and λ_* can both be measured as a function of the applied force f_{ap}. The initial radius R_0 of the specimen, the initial number of fibers per unit volume ν, and the average length of the fiber L between branch points is known. Hence, we can determine $F(\lambda_c)$ which is the force-extension relation of the fibers. Or, if $F(\lambda_c)$ is given then we can predict the force-extension relation of a network specimen. In a subsequent section we will consider a special type of force-extension relation which is suitable when the fiber unfolds under large forces.

Before we move to the next section we also give expressions for another important observable tracked in the experiment – the order parameter $\cos 2\theta$ as a function of the longitudinal stretch λ_1 or the applied force f_{ap}, where θ is the angle made by the $\mathbf{e}_1$-$\mathbf{e}_2$ projection of a fiber to the $\mathbf{e}_1$ direction. In terms of our variables

$$\cos\theta = \frac{\lambda_1}{\sqrt{\lambda_1^2 + \lambda_*^2}}, \tag{17}$$

so that

$$\cos 2\theta = 2\cos^2\theta - 1 = \frac{\lambda_1^2 - \lambda_*^2}{\lambda_1^2 + \lambda_*^2}. \tag{18}$$

Finally, we can also compute the compressibility of the network. The compressibility is defined as

$$K = -\frac{1}{V}\frac{dV}{dP} \tag{19}$$

where V is the current volume of the network and P is the pressure. In our case there is uniaxial tension so that $P = -\frac{1}{3}\mathrm{tr}(\sigma) = -\frac{\sigma_{11}}{3}$ where σ_{11} is a Cauchy stress that has been calculated above. We can write $\frac{dV}{V} = d\left(\frac{V}{V_0}\right)\frac{V_0}{V}$ where V_0 is volume of the network in the reference configuation. But, we recognise that $\frac{V}{V_0} = \lambda_1\lambda_*^2$ is nothing but the relative volume, so that $K = -\frac{1}{\lambda_1\lambda_*^2}\times$ (slope of the relative volume *vs.* pressure curve). For the tensile testing reported here the pressure is negative and we observe a decrease in the clot volume during extension. This leads to a negative compressibility (see main text) for certain values of the strain. Such negative compressibilities, although possibly counterintuitive, are not unprecedented (see, for example,[9, 10]).

Stress-strain behavior of a random network of linear fibers

Consider a random isotropic network of fibers of length L and cross-sectional area A. The force extension relation of the fibers is linear so that

$$F(\lambda_c) = EA(\lambda_c - 1), \tag{20}$$

where E is the Young's modulus. If a network of these fibers is subjected to a uniaxial tension test along the $\mathbf{e}_1$ direction then 'engineering stress' s_{11} can be calculated from (16) as

$$s_{11} = \frac{f_{ap}}{\pi R_0^2} = \frac{\nu LEA}{6}\left(\lambda_1 - \frac{\lambda_*^2}{\lambda_1}\right)\left(1 - \frac{1}{\lambda_c}\right), \qquad \lambda_c = \sqrt{\frac{\lambda_1^2 + 2\lambda_*^2}{3}}. \tag{21}$$

If we further assume that the volume of the network does not change then $\lambda_* = \frac{1}{\sqrt{\lambda_1}}$ and we get

$$s_{11} = \frac{\nu LEA}{6}\left(\lambda_1 - \frac{1}{\lambda_1^2}\right)\left(1 - \frac{1}{\lambda_c}\right), \qquad \lambda_c = \sqrt{\frac{\lambda_1^3 + 2}{3\lambda_1}}. \tag{22}$$

This model seems to be adequate to account for the stress-strain behavior of collagen networks (see Fig. S6) up to a stretch of 1.35. For higher stretches it is possible that some of the fibers already begin to rupture causing the stress to deviate from the predictions of the linear model. The experimental data shown in Fig. S6 is obtained from Roeder *et al.* [11]. They find an average fiber diameter around 435nm and we estimate an average $L \approx 10\mu$m from their images. They do not give estimates of ν or E, but we obtain a good fit to their data if we use $\nu \approx 0.006\mu\mathrm{m}^{-3}$ and $E = 80$MPa [12]. It is interesting to note that the collagen networks studied by Roeder *et al.* [11] were found to rupture at a stretch of about 1.6 which is slightly larger than the stretch $\lambda_1 = 1.5707$, which would result if fibers of equal length oriented randomly in a network were to align with the

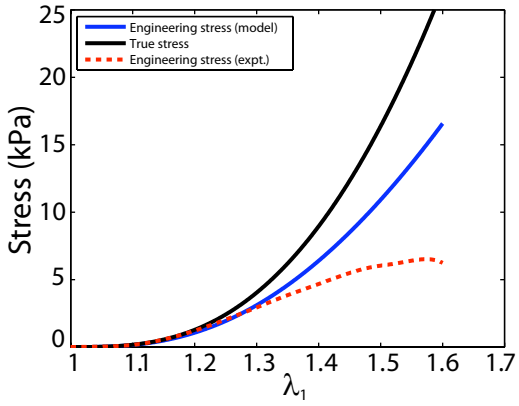

Fig. S 6: Eight-chain model applied to collagen networks. A linear force-extension relation for the collagen fibers seems to be adequate to model the network stress-strain response up to a stretch of about 1.35. The experimental data is obtained from Roeder *et al.* [11]. The solid lines are obtained from the eight-chain model with linear fibers. We use a fiber diameter of 435nm and a length of 10μm. The values of E and ν are less certain but we use $E = 80$MPa and $\nu = 0.006\mu\text{m}^{-3}$ to obtain the solid lines.

$\mathbf{e}_1$ axis. [3] This suggests that most of the strain is accomodated by aligning of the fibers along the loading direction; hence, the fibers do not stretch much, which could be the reason why a linear force-extension relation for collagen fibers is adequate. On the other hand, fibrin networks can sustain much larger strains ($\lambda_1 > 3$) before rupture. The fibrin fibers are known to have Young's moduli around 15MPa [13] and diameters around 200nm which are similar to the values we used for collagen fibers. Our analysis in this section suggests that a linear force-extension relation for fibrin fibers with these parameter values will not be able to give strains around $\lambda_1 = 3$ that we observe in experiments.

Force-extension relation of a fiber with unfolding

When a large force is applied to a fibrin fiber it unfolds. For small forces the force-extension relation is linear. In fact, the Young's modulus E of fibrin fibers in a clot has been measured for small forces and a typical value for ligated fibrin is in the range of $E = 14.5$MPa [13]. Hence, the force-extension relation for fibrin at low forces can be written as

$$x_f = \lambda_f L_f = L_f \left(1 + \frac{F}{EA}\right), \tag{23}$$

where A is the cross-sectional area of the fiber, x_f is the end-to-end distance after deformation, and L_f is the reference (undeformed) length. After unfolding at large forces, fibrin is assumed to behave like a worm-like-chain (WLC) polymer. In this state the force-extension relation is given by

$$x_u = \lambda_u L_u = L_u \left(1 - \frac{\sqrt{k_B T N}}{2\sqrt{\xi_p F}}\right), \tag{24}$$

[3] If all the fibers are of length L and θ is the angle they make with the $\mathbf{e}_1$ axis then $\lambda_1 = L/[\frac{L}{\pi}\int_0^{\pi} |\cos\theta| d\theta] = \pi/2 = 1.5707$.

where ξ_p is a persistence length, N is the number of fibrin molecules making up a single fiber, and L_u is the contour length of the fibrinogen molecules. A similar but much simpler version of such a model had been developed to explain enhanced fluctuations in the red blood cell's spectrin network that could be measured upon cell stretching [14]. We note that the force-extension relation in both phases has been written with F as the independent variable. This is convenient since we will use a two-state equilibrium model in which the fraction of each state is written as a function of the applied force. Our two-state model will have the folded fibrin as the (preferred) low free energy equilibrium state at zero force and the unfolded fibrin as the high free energy equilibrium state at zero force. Let the difference in free-energy between these states be $\Delta\Pi$ and the separation between the energy wells corresponding to these states be Δz. Then the ratio of the number of fibrinogen molecules (which make up a fibrin fiber) in the unfolded state to those in the folded state at equilibrium is

$$\frac{N_u}{N_f} = \exp(-\frac{\Delta\Pi - \frac{F\Delta z}{N}}{k_B T}). \tag{25}$$

Hence, the fractions n_f and n_u of folded and unfolded molecules are respectively

$$n_f = \frac{1}{1+\exp(-\frac{\Delta\Pi - \frac{F\Delta z}{N}}{k_B T})}, \qquad n_u = 1 - n_f. \tag{26}$$

It then follows that the force-extension relation for such a fibrin fiber is given by

$$x = x_f + x_u = n_f(F) L_f \left(1 + \frac{F}{EA}\right) + n_u(F) L_u \left(1 - \frac{\sqrt{k_B T N}}{2\sqrt{\xi_p F}}\right). \tag{27}$$

In terms of the stretch with respect to the (undeformed) reference length of the fibrin fiber we have

$$\lambda = \frac{x}{L_f} = n_f(F) \left(1 + \frac{F}{EA}\right) + n_u(F) \frac{L_u}{L_f} \left(1 - \frac{\sqrt{k_B T N}}{2\sqrt{\xi_p F}}\right). \tag{28}$$

The force-extension relation (28) for a single fibrin fiber is the input to (16) which gives the force-extension relation of the fibrin network. But, this still leaves λ_* undetermined. For a network that does not change volume $\lambda_* = \frac{1}{\sqrt{\lambda_1}}$. But, fibrin networks change their volume when they are subjected to large strains. In order to account for this, we first note that the volume occupied by a network contains both fibers and solvent molecules. Also, the network volume stays constant for stretches greater than 1.7 even though the order paramater $\cos(2\theta)$ (or the shape of the voids) changes in this regime. Based on this observation, we hypothesize that network volume changes occur in parallel with fiber unfolding and not when the fibers are in the fully folded or unfolded state. Assuming further that volume occupied by the fibers and solvent in the folded and unfolded states is proportional to the fractions of folded and unfolded fibrin respectively, we can say that the ratio of volume after deformation to the reference (undeformed) volume is simply

$$\lambda_1 \lambda_*^2 = n_f + C_3 n_u, \tag{29}$$

where C_3 is the ratio of network (fiber + solvent) volumes in the fully folded and fully unfolded configurations. We can combine this equation with $3\lambda_c^2 = \lambda_1^2 + 2\lambda_*^2$ to get the following cubic equation for λ_1:

$$\lambda_1^3 - 3\lambda_1 \lambda_c^2 + 2(n_f + C_3 n_u) = 0. \tag{30}$$

Note that n_f and n_u can be written in terms of λ_c through F. C_3 can be inferred from the experimental data and hence the above is an equation for λ_1 which can be solved by Cardan's method. λ_* can then be determined from (29). Cardan's solution to $\alpha^3 + q\alpha + r = 0$ are the three numbers

$$\alpha = \left(-\frac{r}{2} + \sqrt{\frac{r^2}{4} + \frac{q^3}{27}} \right)^{1/3} + \left(-\frac{r}{2} - \sqrt{\frac{r^2}{4} + \frac{q^3}{27}} \right)^{1/3}. \tag{31}$$

For determining λ_1 we substitute $q = -3\lambda_c^2$ and $r = 2(n_f + C_3 n_u)$.

Three-chain model

The three-chain model can also describe the behavior of random isotropic networks. The framework for obtaining the strain energy density in this model is similar to that for the eight-chain model. The difference lies in the expression for λ_c. If we assume that a cylindrical network is strteched along the $\mathbf{e}_1$ direction, then for the three-chain model:

$$\lambda_c = \lambda_1, \qquad \lambda_2 = \lambda_3 = \lambda_*. \tag{32}$$

If the radius of the cylinder in the reference configuration is R_0 then its deformed radius is $\lambda_* R_0$ and the applied force is given by

$$f_{ap} = \pi \lambda_*^2 R_0^2 \sigma_{11} = \left(\lambda_1 - \frac{\lambda_*^2}{\lambda_1} \right) \frac{\pi R_0^2 \nu L F(\lambda_c)}{6\lambda_c}, \qquad \lambda_c = \lambda_1. \tag{33}$$

And,

$$\lambda_1 = \lambda_c = n_f(F) \left(1 + \frac{F}{EA} \right) + n_u(F) \frac{L_u}{L_f} \left(1 - \frac{\sqrt{k_B T N}}{2\sqrt{\xi_p F}} \right), \tag{34}$$

where n_f and n_u are given by (26) as before. Also, as before λ_* can be computed using (29).

Network parameters and comparison with experiments

The network structural parameters in the unstretched state that are used as inputs for these models are estimated by comparing our electron microscope images and clot formation conditions with earlier detailed measurements of clot structure [16]. At the single-molecule level, force spectroscopy experiments provide an estimate of the free energy difference $\Delta\Pi$, the distance between the energy wells of the folded and unfolded states Δz, and the persistence length of the molecules once they have unfolded; however, since intermolecular interactions in the clot could alter these parameters from their single-molecule values, we have chosen to take the free energy difference and this distance to be free parameters. Force spectroscopy of fibrin protofibrils suggests that while the values of the energy landscape parameters may change, the two-state model of coiled-coil unfolding that was found for end-to-end linked fibrinogen is also applicable to half-staggered side-to-side associated fibrin (Fig. 6).

The fibrin network in our experiments consists of ligated fibers that are assumed to have an average diameter of 185nm and an average length $L = 20\mu$m between branch points. Assuming a Young's modulus of 14.5MPa [13] this corresponds to a stiffness $k = EA = 3.87 \times 10^5$pN in the

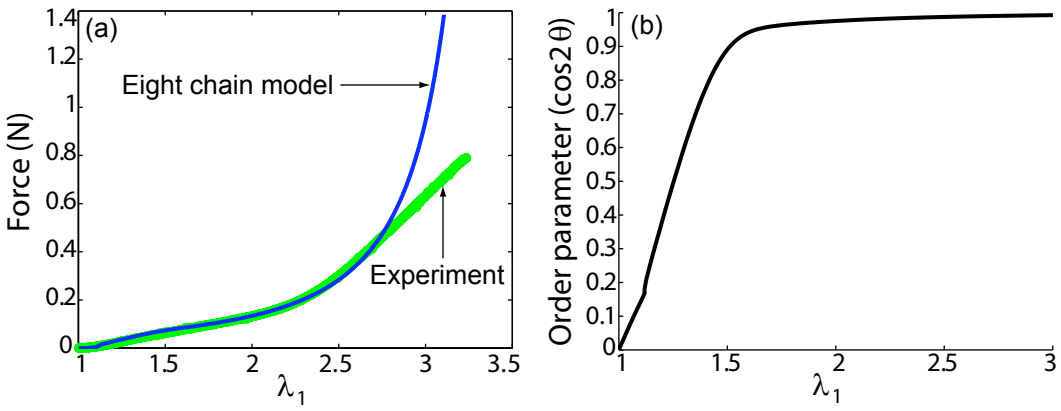

Fig. S 7: Results of the eight-chain model. (a) The force-extension data is reasonably fit with the eight-chain model assuming that a single fibrin fiber behaves linearly (folded state) for low strains and as a WLC (unfolded state) for large strains. The parameters are based on a knowledge of the Young's modulus in the folded state [13] and the persistence length of fibrinogen [15] in the unfolded state. (b) The order parameter $\cos 2\theta$ tends to 1 for large strains. This implies that most of the fibers are aligned with the direction of the applied force at large strains.

folded phase. For the unfolded phase of the individual fibrinogen chains we use $\xi_p = 0.8$nm [15]. The ratio of contour lengths of the fibrinogen chains in the unfolded phase to that in the folded phase, $\frac{L_u}{L_f} \approx 2.1$, based on the experiments of Brown *et al.* [15]. The fiber density is assumed to be $5 \times 10^{-1} \mu\text{m}^{-3}$ and the initial radius, R_0, of the specimens is about 1mm, so that $\frac{\pi R_0^2 \nu L}{6} \approx 10^{-5}$ (see eqn.(16)). In the experiments we observe a dramatic reduction in the volume of the network after deformation. The volume of the fully unfolded network is about 10% of the volume in the reference configuration, so that $C_3 \approx 0.1$.

We need an estimate for N, the number of fibrin molecules (protofibrils) making up a fibrin fiber. We assume that the protofibrils have a circular cross-section of diameter d and are packed in such a way that the cross-section of each protofibril is surrounded by six other protofibrils making up a hexagonal lattice over the diameter D of the fibrin fiber. The protofibrils are loosely packed since the fibrin fibers have 20% protein content. But, if we assume, for the sake of simplicity, that the protofibrils are close packed then from elementary geometry we know that the fraction of area occupied by the cross-sections of the close packed protofibrils is $\frac{\pi}{2\sqrt{3}}$. Hence, we estimate $N = \frac{\pi}{2\sqrt{3}} \frac{D^2}{d^2}$. If we assume that only 20% of the area is occupied by protofibrils then $N = 0.2 \frac{D^2}{d^2}$. We chose an average value of $D = 185$nm. We can obtain estimates for d either from micrographs or from a knowledge of its molecular weight which is 340,000 g/mole. Taking a canonical value of 0.73 cm^3/g for the specific volume of proteins we estimate the volume occupied by a single fibrinogen molecule is 410nm^3. Fibrin molecules in the protofibril are half-staggered, so that there are two half molecules or the equivalent of one full molecule in each repeat of 22.5nm. Thus, the fibrinogen molecule can be thought of as a cylinder of height $h = 22.5$nm [15] and diameter d so that $\pi \frac{d^2}{4} = 410/22.5$, which gives $d \approx 5$nm. Similar estimates of protofibril diameter can be obtained from the crystal structure of fibrinogen [17] and estimates of the packing of protofibrils within the fiber [18, 19]. From this we estimate $N \approx 1240$. We use a value for $N \approx 1200$ in all our calculations.

This leaves the free energy difference $\Delta\Pi$ and the separation Δz as fitting parameters. We find that $\Delta\Pi = 16.5kT$ and $\Delta z = 19.2$nm fits the force-extension data reasonably well except for very large strains (see Fig. S7(a)). The same parameters also fit the data for volume change as a function of λ_1 as seen from Fig. S8(b). Also shown in these figures are the order parameter (Fig. S7(b)) and the fraction of folded and unfolded fibrinogen molecules (Fig. S8(a)) as functions of λ_1.

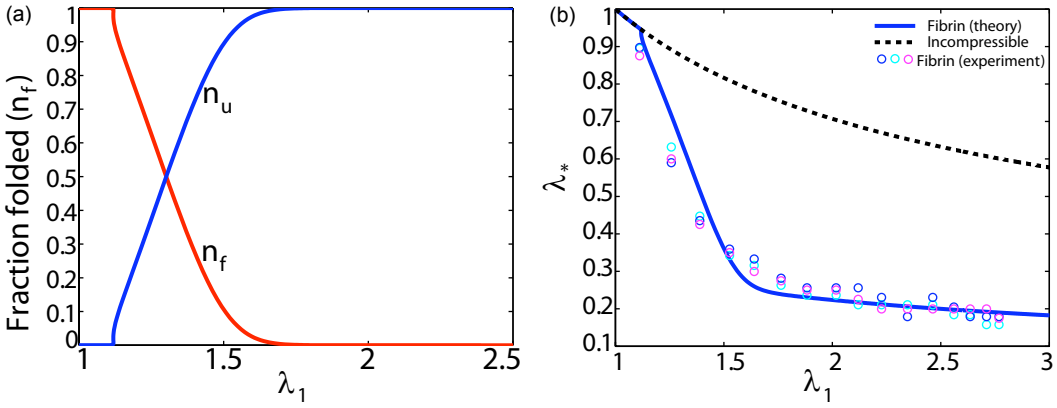

Fig. S 8: Change in the network volume. (a) At low strains there is no unfolding in the fibrin fiber as indicated by the folded fraction n_f. Most of the fibers are completely unfolded at a stretch of 1.8. (b) The transverse stretch λ_* determines the volume change in the network through the expression $\lambda_1\lambda_*^2$ which is the ratio of current to reference volume. The curve is generated assuming $\lambda_1\lambda_*^2 = n_f + 0.1n_u$ where n_f and n_u are the fraction of folded and unfolded fibrinogen molecules. The transverse stretch for an incompressible material is also shown as a function of λ_1. Fibrin seems to behave like an ultra-compressible material due to protein unfolding.

We also checked how well a three-chain model can fit the data for a similar set of parameters as used for the eight-chain model. In particular, we used $k = 3.87 \times 10^5$pN, $\xi_p = 0.8$nm, $\frac{L_u}{L_f} = 3.12$, $\Delta\Pi == 19.2kT$, $\Delta z = 15.2$nm while ν, R_0, N and L are exactly the same as in the eight-chain model. The results of this exercise appear in Fig. S9 and suggest that the three-chain model can also give reasonable fits to the data force as well as volume change as a function of applied stretch.

A few comments about the observed volume change and its relation to unfolding are in order. We measure the fraction of cross-sectional area occupied by the fibers and observe bundling at large values of λ_1 (see Fig. 3D of the main text). For instance, if A_i is the total cross-sectional area of the fibers at $\lambda_1 = 1$ (and $\lambda_* = 1$), we find $\frac{A_i}{\pi R_0^2} = 0.08$. Similarly, if A_f is the total area of cross-section of the fibers at $\lambda_1 = 3.0$ (and $\lambda_* \approx 0.2$), we find $\frac{A_f}{\pi\lambda_*^2 R_0^2} \approx 0.38$. This implies that $\frac{A_f}{A_i} \approx 0.19$. If the total volume occupied by the fibrin fibers did not change (as would be the case with no unfolding) then we would expect that $\frac{A_f}{A_i} = \frac{1}{\lambda_f}$ where λ_f is an average stretch of the fibers. Since the fibers are nearly aligned with the $\mathbf{e}_1$ axis at $\lambda_1 = 3.0$ (see Fig. 3C of main text) we could take $\lambda_f \approx 3.0$ which gives $\frac{A_f}{A_i} \approx 0.33$ if the fiber volume did not change. Based on the eight-chain model, we could also choose $\lambda_f = \lambda_c = \sqrt{(\lambda_1^2 + 2\lambda_*^2)/3} \approx 1.74$ and get $\frac{A_f}{A_i} \approx 0.57$ if the volume of the fiber did not change. The number obtained from our measurement is much smaller than this, implying that the amino-acids constituting the fibers have undergone some spatial rearrangment to

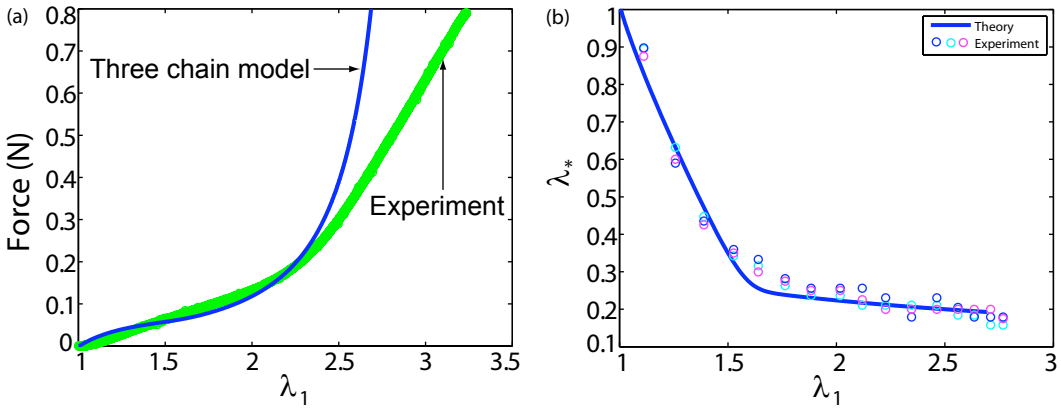

Fig. S 9: Results of the three-chain model. (a) We obtain reasonable fits to the force-extension data using a three-chain model with parameters similar to those used for the eight-chain model. The Young's modulus of the fibers in the folded state, the persistence length of fibrinogen in the unfolded state, the network density and the free energy difference $\Delta\Pi$ used in in this calculation are exactly the same as those used in the eight-chain model. (b) The data for transverse stretch are also well fit by the same parameters.

occupy a smaller volume at large stretches. This is consistent with our idea that the fibrin fibers unfold at large stretches.

Isotropic network model

Isotropic networks of fibers can also be studied using the model of Storm *et al.* [4]. According to this model the Cauchy stress σ_{ij} is given by

$$\sigma_{ij} = \frac{\nu}{det(\mathbf{F})} \langle F(|\mathbf{Fr}|) \frac{F_{il} r_l F_{jk} r_k}{|\mathbf{Fr}|} \rangle_{P(\mathbf{r})}, \tag{35}$$

where ν is the number of fibers per unit volume, $F(|\mathbf{Fr}|)$ is the force-extension relation of individual fibers, and $P(\mathbf{r})$ is the probability distribution function for end-to-end vectors $\mathbf{r}$ of the fibers in the unstressed configuration. We will assume that the end-to-end vectors $\mathbf{r}$ in the unstressed configuration are all such that $|\mathbf{r}| = L$ which is the unstressed length of the fibers in the folded state. Assuming a spherical coordinate system, this means that $P(\mathbf{r}) = P(r, \phi, \theta)$ is independent of the ϕ and θ and is a delta function centered around $r = L$. Assuming a cylindrical specimen with the axis $\mathbf{e}_1$ pointing along the direction of the applied force we write the components of the deformation gradient tensor:

$$F_{11} = \lambda_1, \qquad F_{22} = F_{33} = \lambda_*, \qquad F_{12} = F_{13} = F_{23} = 0. \tag{36}$$

By expanding the expression for the stress we see that the normal stresses are

$$\sigma_{11} = \frac{\nu}{\lambda_1 \lambda_*^2} \langle F(\sqrt{\lambda_1^2 r_1^2 + \lambda_*^2 (r_2^2 + r_3^2)}) \frac{\lambda_1^2 r_1^2}{\sqrt{\lambda_1^2 r_1^2 + \lambda_*^2 (r_2^2 + r_3^2)}} \rangle_{P(\mathbf{r})}, \tag{37}$$

$$\sigma_{22} = \frac{\nu}{\lambda_1 \lambda_*^2} \langle F(\sqrt{\lambda_1^2 r_1^2 + \lambda_*^2 (r_2^2 + r_3^2)}) \frac{\lambda_*^2 r_2^2}{\sqrt{\lambda_1^2 r_1^2 + \lambda_*^2 (r_2^2 + r_3^2)}} \rangle_{P(\mathbf{r})}, \tag{38}$$

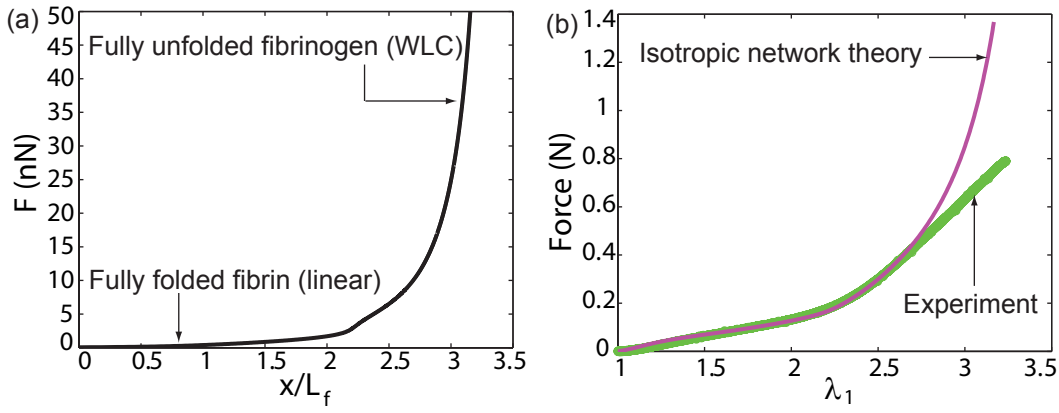

Fig. S 10: Results of the isotropic network model. (a) The force-extension relation for an individual fibrin fiber with unfolding, and properties $EA = 1.0 \times 10^3$pN, $\xi_p = 2.2$nm and $\frac{L_u}{L_f} = 3.53$. (b) The network force-extension curve resulting from using the λ_*–λ_1 relation shown in Fig. S8(b) and the force-extension relation shown in Fig. S10(a) as an input to the isotropic network model. The fit is as good as the one obtained from the eight-chain model and shown in Fig. S7(a). The reason for the low value of k used in this figure is our unrealistic assumption that fibers behave linearly in compression. Allowing for buckling of fibers in compression and using $k = 3.87 \times 10^5$pN gives force-extension curves that are close to the one above (see Fig. S11).

$$\sigma_{33} = \frac{\nu}{\lambda_1\lambda_*^2}\langle F(\sqrt{\lambda_1^2 r_1^2 + \lambda_*^2(r_2^2+r_3^2)})\frac{\lambda_*^2 r_3^2}{\sqrt{\lambda_1^2 r_1^2 + \lambda_*^2(r_2^2+r_3^2)}}\rangle_{P(\mathbf{r})}, \tag{39}$$

Similarly, the shear stresses are given by

$$\sigma_{21} = \frac{\nu}{\lambda_1\lambda_*^2}\langle F(\sqrt{\lambda_1^2 r_1^2 + \lambda_*^2(r_2^2+r_3^2)})\frac{\lambda_1 r_1 \lambda_* r_2}{\sqrt{\lambda_1^2 r_1^2 + \lambda_*^2(r_2^2+r_3^2)}}\rangle_{P(\mathbf{r})}, \tag{40}$$

$$\sigma_{31} = \frac{\nu}{\lambda_1\lambda_*^2}\langle F(\sqrt{\lambda_1^2 r_1^2 + \lambda_*^2(r_2^2+r_3^2)})\frac{\lambda_1 r_1 \lambda_* r_3}{\sqrt{\lambda_1^2 r_1^2 + \lambda_*^2(r_2^2+r_3^2)}}\rangle_{P(\mathbf{r})}, \tag{41}$$

$$\sigma_{32} = \frac{\nu}{\lambda_1\lambda_*^2}\langle F(\sqrt{\lambda_1^2 r_1^2 + \lambda_*^2(r_2^2+r_3^2)})\frac{\lambda_*^2 r_2 r_3}{\sqrt{\lambda_1^2 r_1^2 + \lambda_*^2(r_2^2+r_3^2)}}\rangle_{P(\mathbf{r})}. \tag{42}$$

From a knowledge of the probability distribution function $P(\mathbf{r})$ we are constrained to pick (r_1, r_2, r_3) on the surface of sphere of radius L. Hence, we take

$$r_1 = L\cos\phi, \qquad r_2 = L\sin\phi\sin\theta, \qquad r_3 = L\sin\phi\cos\theta, \tag{43}$$

where $0 \le \phi \le \pi$ and $0 \le \theta \le 2\pi$. Then we can immediately write for the normal stresses

$$\sigma_{11} = \frac{\nu L\lambda_1^2}{4\pi\lambda_1\lambda_*^2}\int_0^{\pi}\int_0^{2\pi} F(\sqrt{\lambda_1^2\cos^2\phi + \lambda_*^2\sin^2\phi})\frac{\cos^2\phi\sin\phi}{\sqrt{\lambda_1^2\cos^2\phi + \lambda_*^2\sin^2\phi}}\,d\theta\,d\phi, \tag{44}$$

$$\sigma_{22} = \frac{\nu L \lambda_*^2}{4\pi\lambda_1\lambda_*^2}\int_0^{\pi}\int_0^{2\pi} F(\sqrt{\lambda_1^2\cos^2\phi+\lambda_*^2\sin^2\phi})\frac{\sin^3\phi\sin^2\theta}{\sqrt{\lambda_1^2\cos^2\phi+\lambda_*^2\sin^2\phi}}\,d\theta\,d\phi, \quad (45)$$

$$\sigma_{33} = \frac{\nu L \lambda_*^2}{4\pi\lambda_1\lambda_*^2}\int_0^{\pi}\int_0^{2\pi} F(\sqrt{\lambda_1^2\sin^2\phi+\lambda_*^2\cos^2\phi})\frac{\sin^3\phi\cos^2\theta}{\sqrt{\lambda_1^2\cos^2\phi+\lambda_*^2\sin^2\phi}}\,d\theta\,d\phi, \quad (46)$$

And for the shear stresses we see that

$$\sigma_{21} = \frac{\nu L \lambda_1\lambda_*}{4\pi\lambda_1\lambda_*^2}\int_0^{\pi}\int_0^{2\pi} F(\sqrt{\lambda_1^2\cos^2\phi+\lambda_*^2\sin^2\phi})\frac{\cos\phi\sin^2\phi\sin\theta}{\sqrt{\lambda_1^2\cos^2\phi+\lambda_*^2\sin^2\phi}}\,d\theta\,d\phi, \quad (47)$$

$$\sigma_{31} = \frac{\nu L \lambda_1\lambda_*}{4\pi\lambda_1\lambda_*^2}\int_0^{\pi}\int_0^{2\pi} F(\sqrt{\lambda_1^2\cos^2\phi+\lambda_*^2\sin^2\phi})\frac{\cos\phi\sin^2\phi L\cos\theta}{\sqrt{\lambda_1^2\cos^2\phi+\lambda_*^2\sin^2\phi}}\,d\theta\,d\phi, \quad (48)$$

$$\sigma_{32} = \frac{\nu L \lambda_*^2}{8\pi\lambda_1\lambda_*^2}\int_0^{\pi}\int_0^{2\pi} F(\sqrt{\lambda_1^2\sin^2\phi+\lambda_*^2\cos^2\phi})\frac{\sin^3\phi\sin 2\theta}{\sqrt{\lambda_1^2\cos^2\phi+\lambda_*^2\sin^2\phi}}\,d\theta\,d\phi, \quad (49)$$

with $\sigma_{21}=\sigma_{31}=\sigma_{32}=0$. The shear stresses are zero as expected but the normal stresses σ_{22} and σ_{33} are not. However, we remember that the volume of the network changes as a function of the applied stretch due to unfolding. We assume here that the function describing the change in volume with λ_1 is known, or equivalently, λ_* is known as a function of λ_1. Hence, the stresses are determined only up to a hydrostatic component $p(\lambda_1)\mathbf{I}$. The pressure $p(\lambda_1)$ is determined by the condition that $\sigma_{22}=\sigma_{33}=0$ since there are no forces applied in the $\mathbf{e}_2$ and $\mathbf{e}_3$ directions. Accounting for this fact and integrating over θ in (44), (45) and (46) we are left with

$$\sigma_{11} = \frac{\nu L \lambda_1}{2\lambda_*^2}\int_0^{\pi} F(\sqrt{\lambda_1^2\cos^2\phi+\lambda_*^2\sin^2\phi})\frac{\cos^2\phi\sin\phi}{\sqrt{\lambda_1^2\cos^2\phi+\lambda_*^2\sin^2\phi}}\,d\phi + p, \quad (50)$$

$$\sigma_{22}=\sigma_{33} = \frac{\nu L}{4\lambda_1}\int_0^{\pi} F(\sqrt{\lambda_1^2\cos^2\phi+\lambda_*^2\sin^2\phi})\frac{\sin^3\phi}{\sqrt{\lambda_1^2\cos^2\phi+\lambda_*^2\sin^2\phi}}\,d\phi + p \quad (51)$$

The final integration over ϕ can be done numerically as follows. For each ϕ and given λ_1 we find a F such that (28) is satisfied with $\lambda^2=\lambda_1^2\sin^2\phi+\lambda_*^2\cos^2\phi$. Then we plug this F into the integrands and compute the sum over all values of ϕ. By repeating this procedure for all values of λ_1 we will be able to plot the stress-stretch relation. p is determined by setting $\sigma_{22}=0$. Hence, we see that the applied force

$$f_{ap} = \pi R_0^2\lambda_*^2\sigma_{11} = \pi R_0^2\nu L\int_0^{\pi}\frac{F(\sqrt{\lambda_1^2\cos^2\phi+\lambda_*^2\sin^2\phi})}{\sqrt{\lambda_1^2\cos^2\phi+\lambda_*^2\sin^2\phi}}\left(\frac{\lambda_1}{2}\cos^2\phi\sin\phi-\frac{\lambda_*^2}{4\lambda_1}\sin^3\phi\right)d\phi. \quad (52)$$

Note that $\lambda_*\le\lambda\le\lambda_1$, where we know that $\lambda_*<1$. This means that for some values of ϕ we will get $\lambda<1$ which in turn implies that some fibers may be in compression. These fibers could buckle; but in this paper we assume that they simply get compressed and the compressive force is given by the linear force-extension relation of the fully folded fibrin fiber.

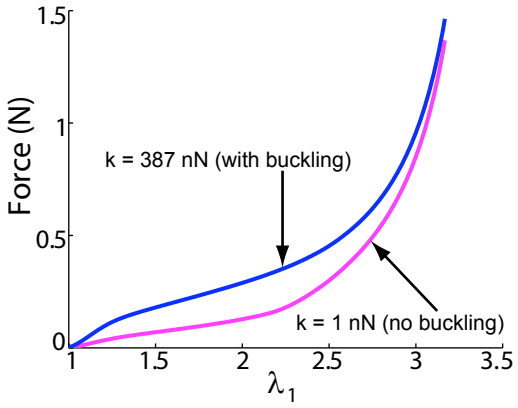

Fig. S 11: Comparison of the force-extension curves predicted by the isotropic network model with and without buckling. Allowing for buckling and setting $k = 3.87 \times 10^5$pN gives curves that are close to curves from Fig. S10(b).

When we carry out the integrations above with the parameter values used in the 'eight-chain model' we find that the network force-extension curve does not capture the trend seen in the experimental data. The experimental data can, however, be fit (except for very large strains) with a different set of values – $k = EA = 1.0 \times 10^3$pN, $\xi_p = 2.2$nm, $\frac{L_u}{L_f} = 3.53$, $\Delta\Pi = 2.0kT$ and $\Delta z = 6.8$nm – while keeping ν, R_0, L and N the same as before. Note that the Young's modulus in the fully folded phase is almost three orders of magnitude smaller in this case. The reason for this is our unrealistic assumption that the fibers behave linearly in compression; instead, setting the force in a fiber to zero for $\lambda < 1$ (to crudely account for buckling) and setting $k = 3.87 \times 10^5$pN (used in the eight-chain and three-chain models) with all other parameters exactly as above leads to force-extension curves that are close to those in the experiment (see Fig. S11). This suggests that allowing for buckling of fibers in compression within the isotropic network model brings its predictions in agreement with those of the eight-chain and three-chain models for similar network parameters.

In summary, the models of both Qi *et al.* [2] and Storm *et al.* [4] are able to capture the trends in the network force-extension data if we account for (a) change in network volume, and (b) the unfolding of individual fibers. The model of Storm *et al.* [4] requires additionally that we set the force in compressed fibers to zero to allow the use of measured fiber stiffnesses to fit the data.

References

[1] Roska F. J., Ferry J. D., Lin J. S., Anderregg, J. W., *Biopolymers* **21**, 1833 (1982).

[2] Qi H. J., Ortiz C. and Boyce M. C., *J. Eng. Mat. Tech.* **128**:509-518 (2006).

[3] James H. M. and Guth E., *J. Chem. Phys.* **11**:455 (1943).

[4] Storm C., Pastore J. J., MacKintosh F. C., Lubensky T. C. and Janmey P. A., *Nature* **435**:191-194 (2005).

[5] Wu P. D. and van der Giessen E., *J. Mech. Phys. Solids* **41**, 427-456 (1993).

[6] Arruda E. M. and Boyce M. C., *J. Mech. Phys. Solids* **41**:389-412 (1993).

[7] Palmer J. S. and Boyce M. C., *Acta Biomat.* **4**:597-612 (2008).

[8] Flory P. J., *Principles of Polymer Chemistry*, Cornell University Press, Ithaca, New York, (1953).

[9] Baughman, R. H., Stafstrm S., Cui C., Dantas S. O., *Science* **279**, 1522 (1998)

[10] Kornblatt A, Sirota E. B., King Jr. H. E., Baughman R. H., Cui S., Stafstrm S. and Dantas S. O. *Science* **281**, 143a-143 (1998).

[11] Roeder B. A., Kokini K., Sturgis J. E., Robinson J. P. and Voytik-Harbin S. L., *Trans. ASME* **124**:214-221 (2002).

[12] Stylianopoulos T. and Barocas V. H., *Comp. Meth. App. Mech.* **196**:2981-2990 (2007).

[13] Collet J.-P., Shuman H., Ledger R. E., Lee S. and Weisel J. W., *Proc. Nat. Acad. Sci. U.S.A.* **102**:9133-9137 (2005).

[14] Lee J. C-M. and Discher D. E., *Biophys. J.* **81**(6), 3178-3192 (2001).

[15] Brown A. E. X., Litvinov R. I., Discher D. E. and Weisel J. W., *Biophys. J.* **92**:L39-L41 (2007).

[16] Ryan E. A., Mockros L. F., Weisel J. W., Lorand L., *Biophys. J.* **77**:2813 (1999).

[17] Kollman J. M., Pandi L., Sawaya M. R., Riley M., Doolittle R. F., *Biochemistry* **48**:3877-3886 (2009).

[18] Voter W. A., Lucaveche C., Erickson H. P., *Biopolymers* **25**:2359-2373 (1986).

[19] Torbet J., Freyssinet J.-M., Hudry-Clergeon G., *Nature* **289**:91-93 (1981).

Movie S1 Caption

Extension of a cylindrical clot with a tensile tester.
A clot prepared as described in the Material and Methods was gently clamped between rubber pads in the grips of a strain-controlled Instron tensile tester equipped with a 2.5 N load cell. The sample was stretched at 10 mm per minute while monitoring the load. This clot was stretched in a bath containing buffer (50 mM Tris-HCl, pH 7.4, 150 mM NaCl, 3 mM $CaCl_2$). The black marks are graphite powder used as fiducial marks on the clot to determine the strain in the center of the sample independent of any effects of clamping. This movie shows the remarkable extensibility of fibrin and the dramatic change in volume that occurs on stretching.